

Low-Frequency Resonance in Strong Heterogeneity

Yinbin Liu
Vancouver, British Columbia, Canada
Email: yliu@eos.ubc.ca

Abstract

Multiple scattering of wave in strong heterogeneity can cause resonance-like wave phenomenon where signal exhibits low-frequency, high intensity, and slowly propagating wave packet velocity. For example, long period event in volcanic seismology and plasmon wave and quantum Hall effect in wave-particle interactions. Collective behaviour in a many-body system is usually thought to be the source for generating the anomalies. However, the detail physical mechanism is not fully understood. Here I show by wave field modeling for microscopic bubble cloud model and 1D heterogeneity that the anomalies are associated with low-frequency resonance in strong small-scale heterogeneity. This low-frequency resonance is a kind of wave coherent scattering enhancement or emergence phenomenon that occurs in transient regime. Its resonance frequency is inversely proportional to heterogeneous scale and contrast and will further shift toward lower frequency with random heterogeneous scale and velocity fluctuations. Low-frequency resonance exhibits the characteristics of localized wave in space and the shape of ocean wave in time and is a ubiquitous wave phenomenon in wave physics.

Introduction

A resonance appears when the frequencies of a driving force match some kind of its own natural frequencies of a system, which exhibits features of selective frequencies and trapped energy. The wavelengths of resonance system are near or smaller than the size of the system. The ringing of a bell is associated with this kind of wave phenomenon.

There is also another kind of ubiquitous observational wave phenomenon in strong small-scale heterogeneity where multiple scattering of wave gives rise to low-frequency anomaly with high intensity and slowly propagating wave packet velocity. Low frequency in this context means the dominant wavelength of signal is much larger than the heterogeneous scale of the system. For example, long period event (1, 2) in volcanic seismology and plasmon wave (3, 4) and quantum Hall effect (5) in wave-particle interactions. The collective behaviour or self-organization and synchronization of a many-body system is generally thought to be the source for generating the low-frequency anomalies. However, the detailed physical mechanism is not quite explicit.

Strong small-scale (or microscopic) heterogeneity is a kind of complex many-body physics system that exhibits the nature of the hierarchical structure of science. The strong nonlinear interaction or multiple scattering among many bodies may emerge an entirely new physical phenomenon that is not understood in terms of a simple extrapolation of the low level structure of the system constituent units (6). Classical multiple wave scattering theory in a many-body system provides a unified theoretical framework for understanding the origin of the macroscopic collective behaviour and revealing the underlying physics of the microscopic constituent interactions. Based on wave field

modelling for microscopic bubble cloud model and 1D heterogeneity, this study shows that multiple scattering of wave in strong small-scale heterogeneity may excite low-frequency resonance (LFR) in transient regime. The low-frequency resonance can provide a simple physical interpretation on the observed resonance-like wave phenomenon in strong small-scale heterogeneity.

Sommerfeld and Brillouin Precursors

An electromagnetic pulse propagating through a single resonance Lorentz dielectric medium will be scattered into high-frequency Sommerfeld precursor and low-frequency Brillouin precursor (7). An acoustic pulse propagating through a bubble cloud medium may also exhibit behaviour similar to Sommerfeld and Brillouin precursors. Fig. 1 shows the acoustic wave field (Figs. 1A to 1D), transmission coefficient (Fig. 1E), and normalized power spectrum (Fig. 1F) of the first cyclic low-frequency wave for acoustic wave scattering by gas-bearing magma medium (8, 9) with different bubble radius and number (see Supplemental material). The other parameters are $\gamma = 1.1$, $\rho_f = 2,700 \text{ kg/m}^3$, $v_f = 1,600 \text{ m/s}$, $P_0 = 2.0 \times 10^5 \text{ Pa}$, $z = 10 \text{ m}$ and 100 m , $b = 0.01 \omega_0$ ($\omega_0 = 2\pi f_0$, f_0 is the Minnaert resonance frequency of a single bubble vibration). Incident wave is a single cycle pulse (solid olive, with a reduced amplitude scale but the same time scale) with the dominant frequency $f_s = 250 \text{ Hz}$ or 20 Hz (dash olive). In numerical integration the principal branch or the first Riemann sheet ($-\pi \leq \arctg[\text{Im}(k^2)/\text{Re}(k^2)] \leq \pi$) is chosen. It can be seen that the total field in Fig. 1A is composed of the early arrival high-frequency small-amplitude wave packet and the late arrival low-frequency large-amplitude wave packet, which are associated with the stopping band feature in Fig. 1E. The former corresponds to Sommerfeld precursor and the latter corresponds to Brillouin precursor in a single resonance Lorentz dielectric medium (7). Sommerfeld precursor exhibits first exponentially increasing oscillation and then exponentially decaying oscillation, and its instantaneous frequency monotonically decreases from infinite (or the maximum frequency of source) to nearby the system resonance frequency. Brillouin precursor exhibits first monotonically increasing and then exponentially decaying oscillation, and its instantaneous frequency monotonically increases from zero to nearby the system resonance frequency. Brillouin precursor behaviours as low-frequency, large-amplitude, and slowly propagating wave packet velocity. It exhibits the shape of ocean wave that can be described by the hyper-Airy function. For short propagation distance, Sommerfeld and Brillouin precursor fields will partly overlap and show the feature of long period event that consists of a high-frequency small-amplitude onset superposing on a low-frequency large-amplitude background in volcanic seismology (1, 2).

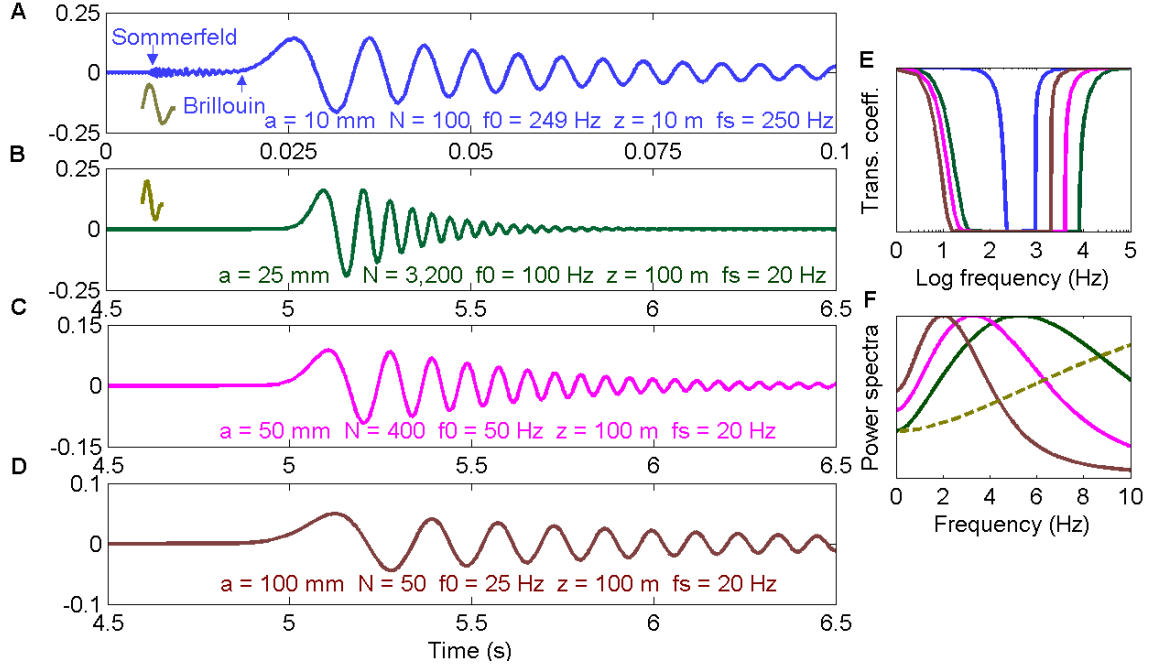


Fig. 1. Acoustic wave scattering by bubble cloud with different bubble radius. **(A)** $N = 100$, $a = 10$ mm, $z = 10$ m, and $f_s = 250$ Hz (blue). **(B)** $N = 3,200$ and $a = 25$ mm (dark green). **(C)** $N = 400$ and $a = 50$ mm (magenta). **(D)** $N = 50$ and $a = 100$ mm (dark red). The propagation distance ($z = 100$ m), the bubble proportion (21%), and the dominant frequency of incident pulse ($f_s = 20$ Hz) are the same for **(B)**, **(C)** and **(D)**. **(E)** Transmission coefficients. **(F)** Normalized power spectra. The spectrum of Brillouin precursor is inversely proportional to the bubble radius.

Figures 1B to 1D show the feature of Brillouin precursor field for different bubble radius but the same bubble proportion (21%) and propagation distance ($z = 100$ m). The larger the bubble radius, the lower the frequency of Brillouin precursor, and the slower the damping. The dominant frequencies of the first cycle Brillouin precursors in Fig. 1F are about 5.3 Hz for $a = 25$ mm (dark green), about 3.3 Hz for $a = 50$ mm (magenta), and about 2.0 Hz for $a = 100$ mm (dark red). The spectra of Brillouin precursors are inversely proportional to the bubble radius and are about one order of magnitude lower (about 19, 15, and 13 times lower) than those of resonance of a single bubble.

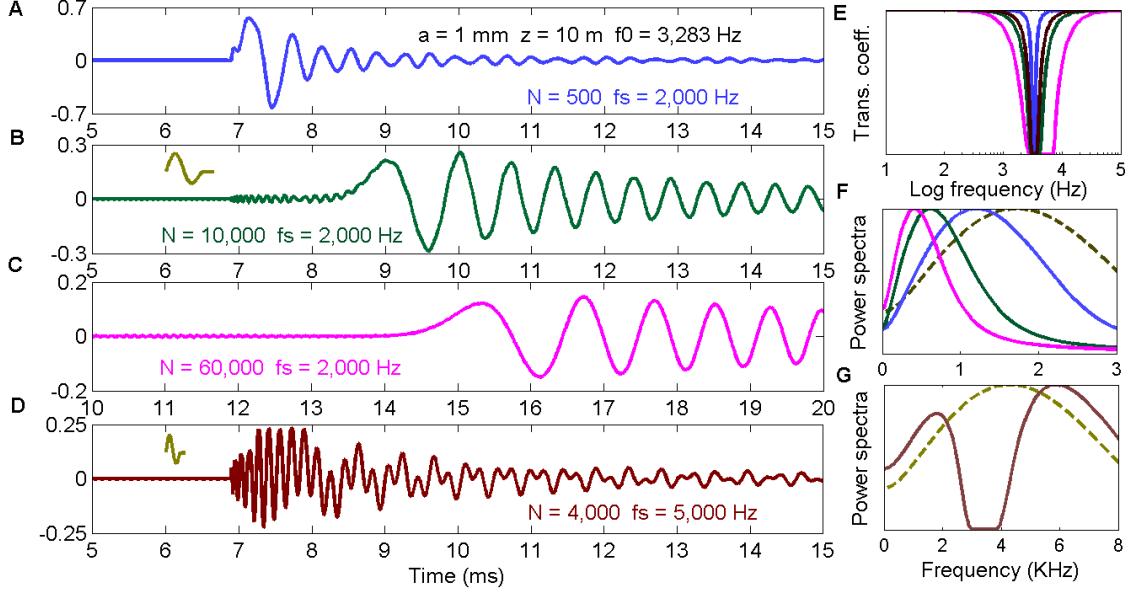


Fig. 2. Acoustic wave scattering by bubble cloud with different bubble proportion. (A) $N = 500$, $\beta = 0.0002\%$, and $f_s = 2,000 \text{ Hz}$ (blue). (B) $N = 10,000$, $\beta = 0.004\%$, and $f_s = 2,000 \text{ Hz}$ (dark green). (C) $N = 60,000$, $\beta = 0.03\%$, and $f_s = 2,000 \text{ Hz}$ (magenta). (D) $N = 4000$, $\beta = 0.002\%$, and $f_s = 5000 \text{ Hz}$ (dark red). (E) Transmission coefficients. (F, G) Normalized power spectra. The spectrum of Brillouin precursor shows a little dependence on bubble proportion.

Figures 2A to 2D shows the acoustic scattering wave field for bubble cloud in water with the same bubble radius ($a = 1 \text{ mm}$) and propagation distance ($z = 10 \text{ m}$) but different bubble proportion (β). The other parameters are $\gamma = 1.4$, $\rho_f = 1,000 \text{ kg/m}^3$, $v_f = 1,450 \text{ m/s}$, $P_0 = 1.013 \times 10^5 \text{ Pa}$, $b = 0.005 \omega_0$. Incident wave is a single cycle pulse (solid olive) with dominant frequency $f_s = 2,000 \text{ Hz}$ (dash olive, Figs. 2A to 2C) or $5,000 \text{ Hz}$ (Fig. 2D). The calculated waveforms are in good agreement with experiment measurements (10). The stopping band in Fig. 2E is much narrower than that in Fig. 1E. The most striking waveform features are a small saw-tooth wave for the early arrival in Fig. 2A and beating phenomenon in Figs. 2D and 2G because of the superposition of Sommerfeld and Brillouin precursor fields. The dominant frequencies of the first cycle Brillouin precursors are about $1,200 \text{ Hz}$ for $\beta = 0.0002\%$, about 620 Hz for $\beta = 0.004\%$, and about 420 Hz for $\beta = 0.03\%$ (Fig. 2F). The frequency of Brillouin precursor field slightly decreases with increasing bubble proportion or decreasing lattice constant. This manifests that Brillouin precursor is much more sensitive to the bubble scale than to the lattice constant. However, bubble proportion has a significant influence on wave packet velocity, which decreases with increasing bubble proportion as shown in Figs. 2A to 2C. This is because the effective velocity of bubble cloud medium ($v_e = \sqrt{K_e/\rho_e}$) is determined by the effective bulk modulus K_e and density ρ_e , and a gas-bearing liquid medium approximately has the bulk modulus close to gas and the density close to liquid.

Low-frequency Resonance in Strong 1D Heterogeneity

For 1D heterogeneity, delta propagator matrix approach (11) can provide an exact analytical solution that includes all multiple scattering effects (see Supplementary material). Two-constituent units embedded between two fluid half-spaces are used to simulate the strong nonlinear interaction in 1D heterogeneity (12, 13). The physical properties of constituent units are shown in Table 1. The strong impedance contrasts for plastic/steel and gas/shale constituents indicate they are strong heterogeneities. Different scale heterogeneities are constructed by varying the lattice constant d while keeping the material proportions and the total thickness. The incident pulse is a single cycle pulse (solid olive in Figs. 3 to 7) with a dominant frequency of $f_s = 172$ Hz (dash olive in Figs. 3 to 7).

Figure 3 shows the normal transmission wave field, the transmission coefficient, and the normalized power spectrum for plastic/steel heterogeneity with a total thickness $D = D_1 + D_2 = 208$ m (32.7% plastic with $D_1 = 68$ m and 67.3% steel with $D_2 = 140$ m) and different lattice constant d that varies from $d = d_1 + d_2 = 52$ m (plastic $d_1 = 17$ m and steel $d_2 = 35$ m) to $d = 3.25$ m (plastic $d_1 = 1.0625$ m and steel $d_2 = 2.1875$ m). The plastic thickness d_1 in plastic/steel heterogeneity is physically equivalent to the bubble radius a in bubble cloud model. The light grey for $d = 52$ m stands for the medium with intrinsic absorption quality factor $Q = 500$, which causes slightly smaller amplitude than that of the corresponding non-absorption medium (blue). The influence of intrinsic absorption will be ignored in the following analysis. The transmission coefficients for 1D heterogeneity in Figs. 3B and 3C are much more complex than those for bubble cloud model in Figs. 1E and 2E. This implies that the solution of the propagator matrix for 1D heterogeneity may include more complex scattering phenomena than those of bubble cloud model.

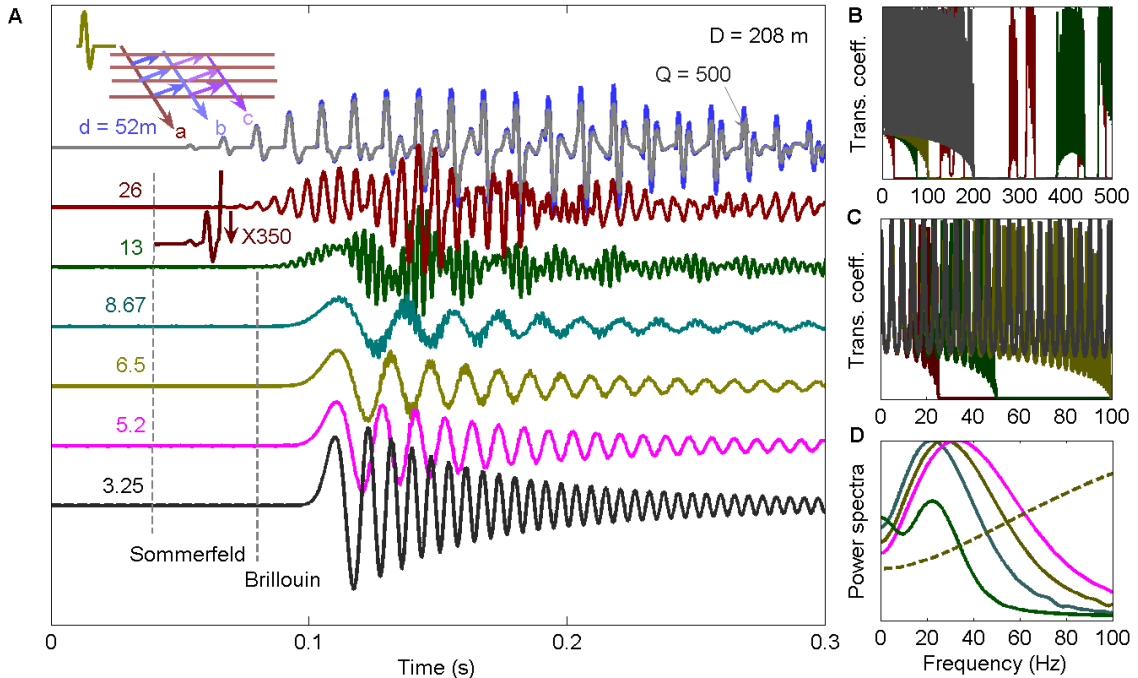


Fig. 3. Scale-dependent low-frequency resonance. Plastic/steel heterogeneity with a total thickness $D = 208$ m and different lattice constant d that varies from $d = 52$ m (8 layers, $d_1 = 17$ m, near seismic wavelength) to $d = 3.25$ m, (128 layers, $d_1 = 1,0625$ m, much less than seismic wavelength). Incident wave is a single cycle pulse (solid olive) with a dominant frequency $f_s = 172$ Hz (dash olive). **(A)** Normal transmission wave field. **(B, C)** Transmission coefficients. **(D)** Normalized power spectra of the first cyclic low-frequency resonance (LFR). The frequencies of LFR are inversely proportional to the lattice constant or heterogeneous scale of medium.

The graphics of the top left in Fig. 3 depicts the direct and the multiple arrivals. The label “a” stands for the direct arrival primary, which has very small amplitude because of the transmission loss. The amplitudes from labels “a” to “b” to “c” gradually increase because “b” and “c” include the constructive interference of many multiple reflections. The local maximum amplitudes of these kinds of arrivals form an envelop with a very slow amplitude change or very low modulation frequency ($d = 52$ m, $d_1 = 17$ m). The waveform with initially exponentially increasing oscillation (“a”, “b”, “c”, *et al.*) exhibits the feature of Sommerfeld precursor field and the low-frequency background exhibits the feature of Brillouin precursor field. As the lattice constant reduces ($d = 26$ m, $d_1 = 8.5$ m), the amplitudes of the first several arrivals (the direct wave and the follows) are very small and the very weak direct wave (the first arrival) is only visible by multiplying an amplified factor of 350. The amplitude of the direct wave becomes negligible and the multiple waves become the first arrival (the behaviour of Sommerfeld precursor field), and the corresponding envelop exhibits a little bit more rapidly changing amplitude or higher modulation frequency. As the lattice constant further reduces ($d = 13$ m, $d_1 = 4.25$ m), the envelop gradually transfers into a real low-frequency component superposed on a high-frequency component (high-frequency onset). For smaller lattice constants ($d = 8.67$ m or $d_1 = 2.83$ m to $d = 3.25$ m or $d_1 = 1.0625$ m), the low-frequency component will transfer into a low-frequency primary with a very slowly raising edge. Its instantaneous frequency increases and amplitude decreases with increasing propagation time, which exhibits the feature of the hyper-Airy function (the behaviour of Brillouin precursor field). Finally the low-frequency wave will transfer into a direct transmission wave in an equivalent transversely isotropic medium for very small lattice constant $d \leq 0.2$ m (13).

The normalized power spectra of the first cyclic low-frequency component for different lattice constant ($d_1 = 4.25$ m, 2.83 m, 2.125 m, and 1.7 m) in Fig. 3A are shown in Fig. 3D. The dominant frequencies are about 22.5 Hz for $d_1 = 2.83$ m (dark cyan), about 27.5 Hz for $d_1 = 2.125$ m (dark olive green), and about 32.5 Hz for $d_1 = 1.7$ m (the magenta). Obviously, the frequencies are inversely proportional to the lattice constant or heterogeneous scale. From a microscopic viewpoint, the low-frequency component is due to the coherent scattering enhancement of multiple scattering waves in strong small-scale heterogeneity, which exhibits resonance-like wave phenomenon with high intensity and scale-dependent frequency in macroscopic scale. I call this phenomenon low-frequency resonance (LFR), which is a kind of collective behaviour or emergence phenomenon that

occurs in transient regime. Modeling also demonstrates that the frequency of LFR slightly decreases with increasing plastic proportion (the softer constituent unit) for the same lattice constant in 1D heterogeneity. However, this kind of scale effect of soft constituent is much weaker than that of bubble cloud model. Note that the concept of LFR is different from that of acoustic resonance scattering generated by the excitation of resonance or creeping wave of a single body during scattering process (14).

The above analysis shows that the high-frequency component and LFR can be approximately seen as Sommerfeld and Brillouin precursor fields, respectively. Sommerfeld precursor is predominant for large heterogeneous scale and Brillouin precursor is predominant for small heterogeneous scale. In moderate heterogeneous scale, the two kinds of precursor fields are both important. From the viewpoint of hierarchical structures, Sommerfeld precursor can be seen as an emergence of physical property in the low level structure and Brillouin precursor as that in the high level structure of the system. The shift from the low to the high level structures is continuous because Sommerfeld and Brillouin precursors occurred in different hierarchical structures obey the same fundamental physics laws.

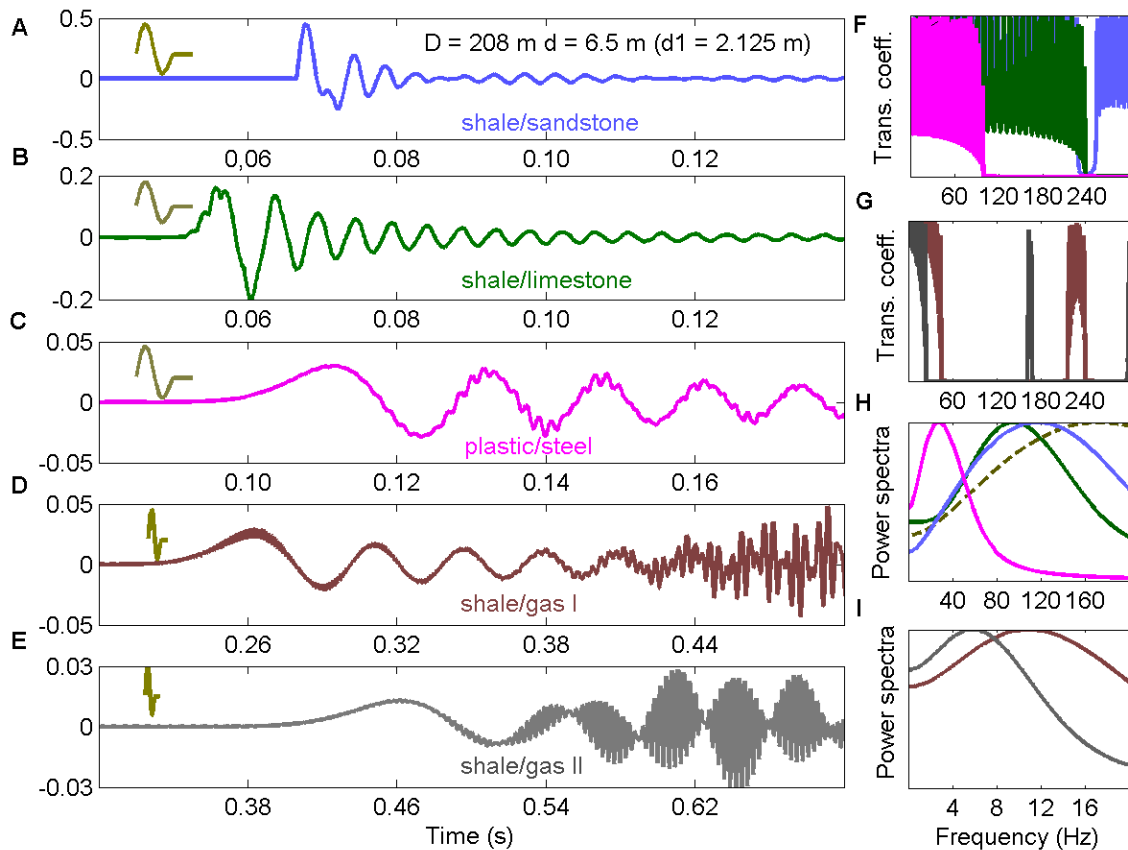


Fig. 4. Contrast-dependent low-frequency resonance. 1D heterogeneity with the same lattice constant $d = 6.5$ m ($d_1 = 2.125$ m) and total thickness $D = 208$ m and different constituents. (A – E) Normal transmission wave fields for shale/sandstone heterogeneity (blue), shale/limestone heterogeneity (dark green), plastic/steel heterogeneity (magenta), shale/gas I heterogeneity (dark red), and shale/gas II heterogeneity (grey). (F, G)

Transmission coefficients. **(H, I)** Normalized power spectra. The frequency of low-frequency resonance decreases with increasing impedance contrast of medium.

Figure 4 shows the normal transmission wave field, transmission coefficient, and normalized power spectrum for 1D heterogeneity with the same lattice constant $d = 6.5$ m ($d_1 = 2.125$ m) and total thickness $D = 208$ m and five kinds of impedance contrasts. The larger the impedance contrast, the lower the frequency of the first stopping band occurs, and the wider the stopping band. This causes complex signal distortion in Figs. 4A to 4E. The frequencies of the first cyclic LFR are about 116 Hz for shale/sandstone heterogeneity, 95.5 Hz for shale/limestone heterogeneity, 27.5 Hz for plastic/steel heterogeneity, 11 Hz for shale/gas I heterogeneity, and 6 Hz for shale gas II heterogeneity. The frequency of LFR decreases with increasing impedance contrast of constituent units. The high-frequency small-amplitude saw-tooth waves superposing on the low-frequency background in Figs. 4B, 4D and 4E are mainly associated with the resonances of individual constituent units. The fundamental resonance frequencies are $f_0 = v_p/2d_1 = 235$ Hz for gas I and 165 Hz for gas II and $f_0 = v_p/2d_2 = 323$ Hz for shale. The resonance strength of the shale layer is much smaller than that of the gas layer because a low-velocity layer can trap more seismic energy. The resonance frequencies of an individual gas layer are about 20 times for shale/gas I heterogeneity and 27 times for shale gas II heterogeneity higher than the corresponding frequencies of LFR.

Figure 5 shows the normal transmission wave field, normalized power spectrum, and transmission coefficient for plastic/steel heterogeneity with a lattice constant $d = 6.5$ m ($d_1 = 2.125$ m) and four total thicknesses. The first stopping bands in Figs. 5B and 5C occur from about 100 Hz to about 500 Hz for the same lattice constant but different total thicknesses. However, the rapid oscillation of transmission coefficient is dependent on the total thickness; the thinner the total thickness, the faster the oscillation. The frequencies of the first cyclic low-frequency resonance are about 27.5 Hz for $D = 208$ m, 24.5 Hz for $D = 312$ m, 22.5 Hz for $D = 416$ m, and 21 Hz for $D = 520$ m, and their amplitude also slightly decrease with the increasing total thickness. The longer the propagation distance, the smaller the changes of both the frequency and intensity of LFR. This indicates the low-frequency resonance is a kind of local resonance effect and basically independent on the total thickness (or total volume) of medium. This kind of localized wave is different from the classical Anderson's wave localization (15). The former exhibits scattering propagation behaviour with no scattering attenuation or superconductivity-like propagation effect and the latter is mainly associated with scattering diffusion behaviour with very small diffusion constant or no diffusion.

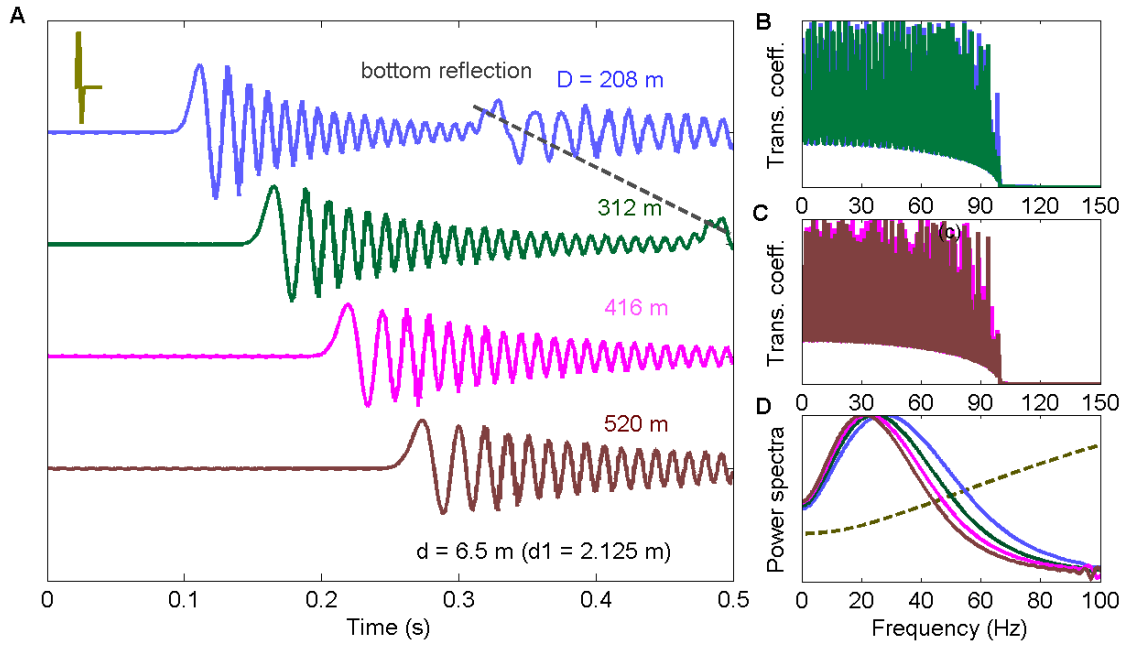


Fig. 5. Volume-independent low-frequency resonance. Plastic/steel heterogeneity with a lattice constant $d = 6.5$ m ($d_1 = 2.125$ m) and four total thicknesses $D = 208$ m (blue, 64 layers), $D = 312$ m (dark green, 96 layers), $D = 416$ m (magenta, 128 layers), and $D = 520$ m (dark red, 160 layers). The straight dash grey denotes the reflections from the bottom fluid half-space. (A) Normal transmission wave fields. (B, C) Transmission coefficients. (D) Normalized power spectra. The low-frequency resonance is basically independent of the total thickness of medium.

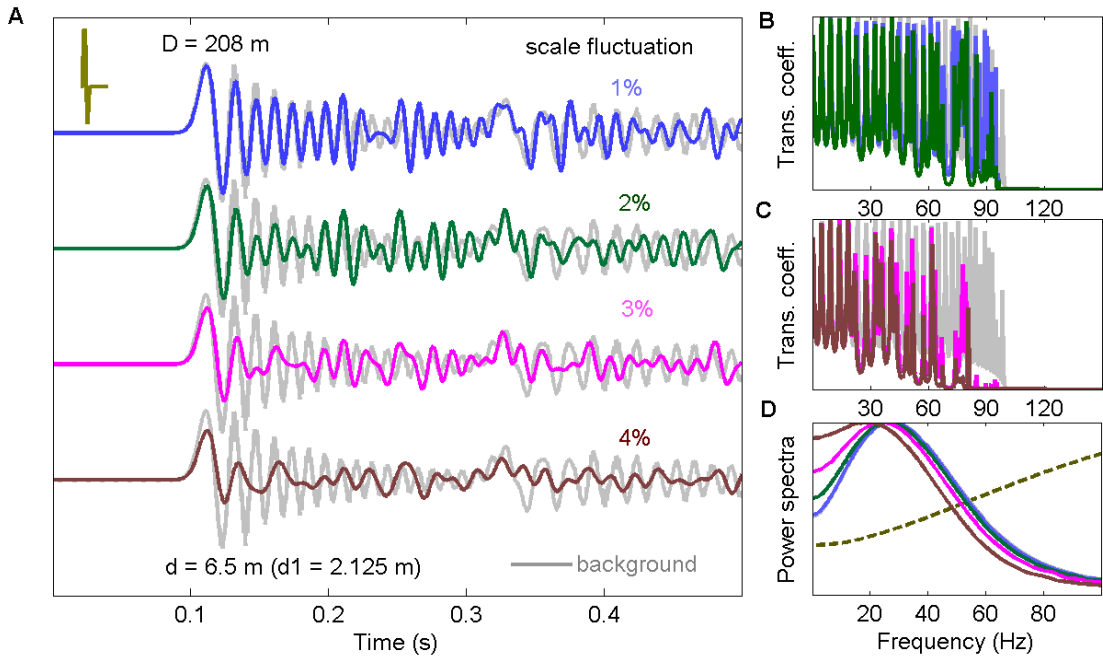


Fig. 6. Effect of random scale fluctuation on low-frequency resonance. Plastic/steel heterogeneity with lattice constant $d = 6.5$ m ($d_1 = 2.125$ m), total thickness $D = 208$ m, and different RMS scale fluctuations. **(A)** Normal transmission wave fields for the scale fluctuations $\delta d/d = 1\%$ (blue), 2% (dark green), 3% (magenta), and 4% (dark red). **(B, C)** Transmission coefficients. **(D)** Normalized power spectra. The frequency of low-frequency resonance decreases with increasing scale fluctuation.

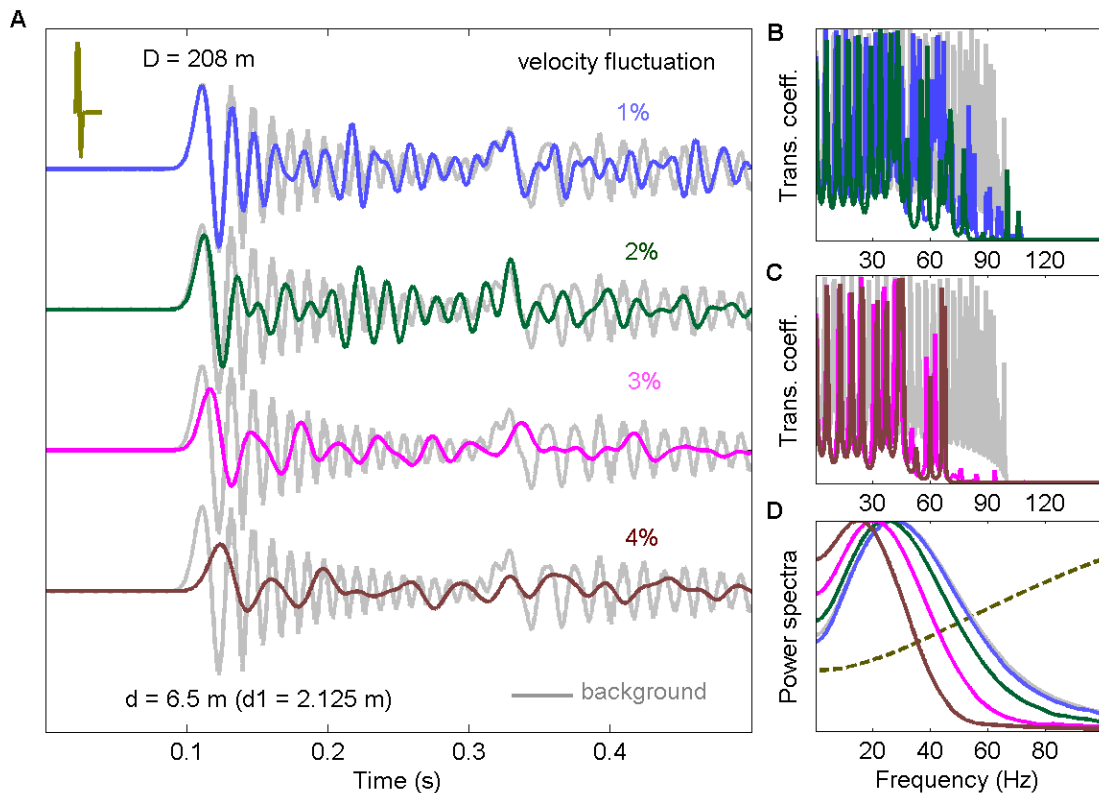


Fig. 7. Effect of random velocity fluctuation on low-frequency resonance. The same as Fig. 6 except for RMS velocity fluctuations $\delta v/v = 1\%$ (blue), 2% (dark green), 3% (magenta), and 4% (dark red). The frequency of low-frequency resonance decreases with increasing velocity fluctuation.

Figures 6 and 7 show the influence of random scale (Fig. 6) and velocity (Fig. 7) fluctuations of plastic/steel heterogeneity on low-frequency resonance. The fluctuations labeled from 1% to 4% in Figs. 6A and 7A represent the root-mean-square (RMS) scale and velocity fluctuations (the grey for the background), respectively. An increase in the scale and velocity fluctuations means a decrease in the symmetry of small-scale heterogeneity. It can be seen that the first stopping bands in Figs. 6B, 6C, 7B and 7C shift slightly toward lower frequency and the oscillation peaks decrease slightly with the increasing scale and velocity fluctuations. The frequencies of the first cyclic low-frequency resonance are about 27.5 Hz for $\delta d/d = 0\%$ (grey) and 1% (blue), 26.5 Hz for $\delta d/d = 2\%$ (dark green), 24 Hz for $\delta d/d = 3\%$ (magenta), and 19 Hz for $\delta d/d = 4\%$ (dark red) for scale fluctuations in Fig. 6D; and are about 27.5 Hz for $\delta v/v = 0\%$ (grey)

and 1% (blue), 25 Hz for $\delta v/v = 2\%$ (dark green), 20.5 Hz for $\delta v/v = 3\%$ (magenta), and 15 Hz for $\delta v/v = 4\%$ (dark red) for velocity fluctuations in Fig. 7D. The frequency of LFR shifts toward lower frequency with increasing random heterogeneous scale and velocity fluctuations. Figs. 6 and 7 also show the energy of LFR decreasing with increasing scale and velocity fluctuations. These features suggest that the frequency and strength of LFR will decrease with the lowering of the degree of symmetry of small-scale heterogeneity.

Discussion

Low-frequency seismic anomaly is often observed in strong small-scale heterogeneity from pore-scale to fault-scale heterogeneities, for example, hydro-fractures (16), volcanic tremor (16), and non-volcanic tremor (17, 18). LFR or Brillouin precursor provides a simple physical interpretation for the low-frequency phenomena. Low-frequency resonance originates from the interference or coherence among multiple scattering waves and should be a ubiquitous wave phenomenon in wave physics. It is believed that the observed low-frequency anomalies in wave-particle interactions that include electromagnetic, matter, and gravitational waves (3 - 5, 19) are also associated with LFR.

Low-frequency resonance is a kind of collective behaviour or emergence phenomenon caused by multiple wave scattering in strong small-scale heterogeneity. Emergence phenomenon of a many-body system is the origin of many fascinating phenomena in nature with scales ranging from the smallest subatomic particles to the largest universe stars. The classic multiple scattering theory (MST), based on wave equation and boundary conditions, provides exact analytical series solutions for 2D and 3D many-body systems (20). These solutions can be developed to numerically study the microscopic constituent interactions and the macroscopic collective behaviour in more complex 2D and 3D many-body systems. Random matrix theory (RMT) studies the eigenvalue spacing distribution of response matrix for evaluating the symmetries and collectivities of the microscopic constituent units (21). The marriage between MST and RMT may open up new opportunities for understating the microscopic constituent distribution of a complex many-body system.

Tables

Table 1 Physical properties of constituents

Medium	$v_p (m/s)$	$v_s (m/s)$	$\rho (kg/m^3)$
Plastic	2487	1048	1210
Steel	5535	3000	7900
Shale	2743	1509	2380
Sandstone	3353	1844	2300
Limestone	5540	3040	2700
Gas I	1000		400
Gas II	700		250

References and Notes

1. B. Chouet, *Nature* **380**, 309 (1994).
2. K. Aki, V. Ferrazzini, *J. Geophys. Res.* **105**, 16617 (2000).
3. J. Homola, S. Yee, G. Gauglitz, *Sensors & Actuators B* **54**, 3 (1999).
4. C. Gennet, T. W. Ebbesen, *Nature* **445**, 39 (2007).
5. S. J. Ilani *et al.*, *Nature* **427**, 328 (2004).
6. P. W. Anderson, *Science* **177**, 393 (1972).
7. L. Brillouin, *Wave Propagation and Group Velocity* (Academic, New York, 1960).
8. M. Minnaert, *Phil. Mag.* **16**, 235 (1933).
9. N. Q. Lu, A. Prosperetti, S. W. Yoon, *IEEE J. Ocean. Eng.* **15**, 275 (1990).
10. L. Brillouin, *Wave Propagation and Group Velocity* (Academic, New York, 1960).
11. H. Medwin, M. M. Beaky, *J. Acoust. Soc. Am.* **86**, 1124 (1989).
12. J. W. Dunkin, *Bull. Seismol. Soc. Am.* **55**, 335 (1965).
13. D. Marion, T. Mukerji, G. Mavko, *Geophysics* **59**, 1613 (1994).
14. Y. Liu, D. R. Schmitt, *Pure and Appl. Geophys.* **163**, 1327 (2006).
15. Y. Liu, R. S. Wu, C. F. Ying, *Geophys. J. Int.* **142**, 439 (2000).
16. P. W. Anderson, *Phys. Rev.* **109**, 1492 (1958).
17. V. Ferrazzini, B. Chouet, M. Fehler, K. Aki, *J. Geophys. Res.* **95**, 21,871 (1990).
18. K. Obara, *Science* **296**, 1679 (2002).
19. D. Shelly, G. C. Beroza, S. Ide, *Nature* **446**, 305 (2007).
20. The LIGO Scientific Collaboration, and the Virgo Collaboration, arXiv: 1602.03840 (2016).
21. V. Twersky, *J. Opt. Soc. Am.* **52**, 145 (1962).
22. T. A. Brody *et al.*, *Rev. Mod. Phys.* **53**, 385 (1981).

Acknowledgements

I thank Drs. Michael G. Bostock, A. Mark Jellinek, Garry Rogers, Ru-Shan Wu, Doug R. Schmitt, and Ping Sheng for discussion and encouragement. I thank my wife, Xiaoping Sally Dai and my daughter, Wenbo Elissa Liu for their encouragement, understanding, and financial support that keep my inner stability for the past over ten years.

Data and Resources Section

No data were used in this paper.

Supplemental Material: This paper includes an electronic supplement to describe the methods for simulating the scattering wave fields in 3D bubble cloud model and in 1D heterogeneity.

Methods

Bubble Cloud Model

For acoustic wave scattering in bubble cloud medium, based on Foldy's multiple scattering theory, the effective wavenumber (9) and the acoustic wave field in time domain can be written as

$$k^2 = \frac{\omega^2}{v_f^2} \left(1 + \frac{4\pi v_f^2 N a}{\omega^2 + 2i\omega b - \omega_0^2} \right) \quad (S1)$$

$$\omega_0 = 2\pi f_0 = \frac{1}{a} \sqrt{\frac{3\gamma P_0}{\rho_f}} \quad (S2)$$

$$p(z,t) = \frac{1}{2\pi} \text{Re} \int G(\omega) \exp[i(kz - \omega t)] d\omega \quad (S3)$$

where Re means “the real part”, k is the effective wavenumber, and $G(\omega)$ is the spectrum of a plane incident pulse. N , a , ω_0 , b , γ , ρ_f , v_f , and P_0 are the number of bubbles per unit volume, the radius of the bubble, the Minnaert resonance angular frequency (8), damping constant, the ratio of specific heats, the density, the acoustic velocity, and the hydrostatic pressure, respectively.

The transmission coefficients and wave fields for bubble cloud scattering can be calculated by equations (S1) to (S3).

Delta Propagator Matrix Approach

For 1D heterogeneity, propagator matrix approach can provide an exact analytical solution that includes all multiple scattering effects. However, there is computational instability for the reflection and transmission coefficients expressed by the propagator matrix. Delta propagator matrix (11) can improve the instability and will be employed to study the multiple scattering processing in this study.

The displacement and stress matrix can be written as

$$S_0^- = B S_n^+ \quad (S4)$$

$$B = \prod_{i=1}^n B_i \quad (S5)$$

$$B_i = X_i D_i^{-1} X_i^{-1} \quad (S6)$$

where $S = (u_x, u_z, \sigma_{zz}, \sigma_{zx})$ is the displacement and stress vector. X_i , D_i , and B_i are 4×4 matrixes related to medium properties.

$$\mathbf{X}_i = \begin{pmatrix} 1 & 1 & 1 & 1 \\ \xi_{1i} & -1/\xi_{2i} & -\xi_{1i} & 1/\xi_{2i} \\ \rho_i(v^2 - 2\beta_i^2) & -2\rho_i\beta_i^2 & \rho_i(v^2 - 2\beta_i^2) & -2\rho_i\beta_i^2 \\ 2\rho_i\beta_i^2\xi_{1i} & \rho_i(v^2 - 2\beta_i^2)/\xi_{2i} & -2\rho_i\beta_i^2\xi_{1i} & -\rho_i(v^2 - 2\beta_i^2)/\xi_{2i} \end{pmatrix} \quad (\text{S7})$$

$$\mathbf{D}_i = \begin{pmatrix} \exp(ix_{1i}) & 0 & 0 & 0 \\ 0 & \exp(ix_{2i}) & 0 & 0 \\ 0 & 0 & \exp(-ix_{1i}) & 0 \\ 0 & 0 & 0 & \exp(-ix_{2i}) \end{pmatrix} \quad (\text{S8})$$

$$x_{1i} = \omega/v\xi_{1i}d_i \quad (\text{S9})$$

$$x_{2i} = \omega/v\xi_{2i}d_i \quad (\text{S10})$$

$$\xi_{1i} = \sqrt{v^2/\alpha_i^2 - 1} \quad (\text{S11})$$

$$\xi_{2i} = \sqrt{v^2/\beta_i^2 - 1} \quad (\text{S12})$$

where α_i , β_i , and d_i are the compressional and shear velocities and the thickness of layer i , respectively.

The reflection and transmission coefficients can be written as

$$\mathbf{R}(\omega) = (\mathbf{R}_1 - \mathbf{R}_2)/(\mathbf{R}_1 + \mathbf{R}_2) \quad (\text{S13})$$

$$\mathbf{T}(\omega) = -2abb_{41}/(\mathbf{R}_1 + \mathbf{R}_2) \quad (\text{S14})$$

$$\mathbf{R}_1 = \mathbf{a}[\mathbf{b}(\mathbf{b}_{31}\mathbf{b}_{43} - \mathbf{b}_{33}\mathbf{b}_{41}) + \mathbf{a}(\mathbf{b}_{31}\mathbf{b}_{42} - \mathbf{b}_{32}\mathbf{b}_{41})] \quad (\text{S15})$$

$$\mathbf{R}_2 = \mathbf{b}[\mathbf{a}(\mathbf{b}_{21}\mathbf{b}_{42} - \mathbf{b}_{22}\mathbf{b}_{41}) + \mathbf{b}(\mathbf{b}_{21}\mathbf{b}_{43} - \mathbf{b}_{23}\mathbf{b}_{41})] \quad (\text{S16})$$

$$\mathbf{a} = \sqrt{v^2/v_f^2 - 1} \quad (\text{S17})$$

$$\mathbf{b} = \rho_f v^2 \quad (\text{S18})$$

where ρ_f and v_f are the density and velocity of the fluid and v is the phase velocity. The transmission and reflection wave fields for an incident plane pulse with spectrum $G(\omega)$ can be written as

$$p_r(t) = \int_{-\infty}^{\infty} G(\omega)\mathbf{R}(\omega)\exp[i(kx - \omega t)]d\omega \quad (\text{S19})$$

$$p_t(t) = \int_{-\infty}^{\infty} G(\omega)\mathbf{T}(\omega)\exp[i(kx - \omega t)]d\omega \quad (\text{S20})$$

There is inherent computational instability in equations (S19) and (S20). The delta propagator matrix (II) can provide an analytical solution that accurately includes all propagation and scattering effects like multiple scattering, conversion of P and SV waves, and evanescence waves, *et al.*. The 2th-order delta subdeterminants of propagator B in equation (S5) can be written as

$$B_{IJ}^{\Delta} = b_{kl}^{ij} = b_{ik} b_{jl} - b_{il} b_{jk} \quad (S21)$$

where I and J = 1, 2, 3, 4, 5, 6 are corresponding to the paired indices ij or kl = 12, 13, 14, 23, 24, 34, respectively. Thus equations (S15) and (S16) can be expressed by delta matrix as

$$R_1 = a(bb_{62}^{\Delta} + ab_{61}^{\Delta}) \quad (S22)$$

$$R_2 = b(ab_{51}^{\Delta} + bb_{52}^{\Delta}) \quad (S23)$$

The elements of propagator matrix B are

$$b_{11} = b_{44} = \frac{2\beta_i^2 \cos x_{1i} + (v^2 - 2\beta^2) \cos x_{2i}}{v^2} \quad (S24)$$

$$b_{12} = b_{34} = \frac{i[(2\beta_i^2 - v^2) \sin x_{1i} + 2\beta_i^2 \xi_{1i} \xi_{2i}] \sin x_{2i}}{\xi_{1i} v^2} \quad (S25)$$

$$b_{13} = b_{24} = \frac{\cos x_{1i} - \cos x_{2i}}{\rho_i v^2} \quad (S26)$$

$$b_{14} = -i \frac{\sin x_{1i} + \xi_{1i} \xi_{2i} \sin x_{2i}}{\rho_i v^2 \xi_{1i}} \quad (S27)$$

$$b_{21} = b_{43} = i \frac{-2\xi_{1i} \xi_{2i} \beta_i^2 \sin x_{1i} + (v^2 - 2\beta_i^2) \sin x_{2i}}{\xi_{2i} v^2} \quad (S28)$$

$$b_{22} = b_{33} = \frac{(v^2 - 2\beta_i^2) \cos x_{1i} + 2\beta_i^2 \cos x_{2i}}{v^2} \quad (S29)$$

$$b_{23} = -i \frac{\xi_{1i} \xi_{2i} \sin x_{1i} + \sin x_{2i}}{\rho_i v^2 \xi_{2i}} \quad (S30)$$

$$b_{31} = b_{42} = \frac{2\rho_i \beta_i^2 (v^2 - 2\beta_i^2) (\cos x_{1i} - \cos x_{2i})}{v^2} \quad (S31)$$

$$b_{32} = -i \frac{\rho_i (v^2 - 2\beta_i^2)^2 \sin x_{1i} + 4\rho_i \beta_i^4 \xi_{1i} \xi_{2i} \sin x_{2i}}{v^2 \xi_{1i}} \quad (S32)$$

$$b_{41} = -i \frac{4\rho_i \beta_i^4 \xi_{1i} \xi_{2i} \sin x_{1i} + \rho_i (v^2 - 2\beta_i^2)^2 \sin x_{2i}}{v^2 \xi_{2i}} \quad (S33)$$

The elements of delta propagator B^{Δ} are

$$b_{11}^{\Delta} = b_{66}^{\Delta} = \frac{1}{v^4 \xi_{1i} \xi_{2i}} [4\xi_{1i} \xi_{2i} \beta_i^2 (2\beta_i^2 - v^2) (\cos x_{1i} \cos x_{2i} - 1) - (4\beta_i^4 - 4\beta_i^2 v^2 + v^4 + 4\xi_{1i}^2 \xi_{2i}^2 \beta_i^4) \sin x_{1i} \sin x_{2i}] + 1 \quad (S34)$$

$$b_{12}^{\Delta} = b_{56}^{\Delta} = -\frac{i}{\rho_i v^2} (1/\xi_{2i} \cos x_{1i} \sin x_{2i} + \xi_{1i} \sin x_{1i} \cos x_{2i}) \quad (S35)$$

$$\begin{aligned} b_{13}^\Delta = b_{14}^\Delta = b_{36}^\Delta = b_{46}^\Delta &= \frac{1}{\rho_i v^4 \xi_{1i} \xi_{2i}} [\zeta_{1i} \zeta_{2i} (v^2 - 4\beta_i^2) (\cos x_{1i} \cos x_{2i} - 1) \\ &+ (2\beta_i^2 - v^2 + 2\xi_{1i}^2 \xi_{2i}^2 \beta_i^2) \sin x_{1i} \sin x_{2i}] \end{aligned} \quad (\text{S36})$$

$$b_{15}^\Delta = b_{26}^\Delta = -i \frac{1}{\rho_i v^2} (1/\xi_{1i} \sin x_{1i} \cos x_{2i} + \xi_{2i} \sin x_{2i} \cos x_{1i}) \quad (\text{S37})$$

$$b_{16}^\Delta = \frac{1}{\rho_i^2 v^4} \{-2 \cos x_{1i} \cos x_{2i} + [\xi_{1i} \xi_{2i} + 1/(\xi_{1i} \xi_{2i})] \sin x_{1i} \sin x_{2i} + 2\} \quad (\text{S38})$$

$$b_{21}^\Delta = b_{65}^\Delta = -\frac{i\rho_i}{v^2} [4\xi_{2i} \beta_i^4 \cos x_{1i} \sin x_{2i} + 1/\xi_{1i} (4\beta_i^4 - 4\beta_i^2 v^2 + v^4) \sin x_{1i} \cos x_{2i}] \quad (\text{S39})$$

$$b_{22}^\Delta = b_{55}^\Delta = \cos x_{1i} \cos x_{2i} \quad (\text{S40})$$

$$b_{23}^\Delta = b_{24}^\Delta = b_{35}^\Delta = b_{45}^\Delta = \frac{i}{v^2} [2\beta_i^2 \xi_{2i} \cos x_{1i} \sin x_{2i} + (2\beta_i^2 - v^2)/\xi_{1i} \sin x_{1i} \cos x_{2i}] \quad (\text{S41})$$

$$b_{25}^\Delta = \xi_{2i}/\xi_{1i} \sin x_{1i} \sin x_{2i} \quad (\text{S42})$$

$$\begin{aligned} b_{31}^\Delta = b_{64}^\Delta = b_{41}^\Delta = b_{63}^\Delta &= \frac{\rho_i}{v^4 \xi_{1i} \xi_{2i}} [2\zeta_{1i} \zeta_{2i} \beta_i^2 (8\beta_i^4 - 6\beta_i^2 v^2 + v^4) (\cos x_{1i} \cos x_{2i} - 1) \\ &- (6\beta_i^2 v^4 + 8\beta_i^6 - 12\beta_i^4 v^2 - v^6 + 8\xi_{1i}^2 \xi_{2i}^2 \beta_i^6) \sin x_{1i} \sin x_{2i}] \end{aligned} \quad (\text{S43})$$

$$b_{32}^\Delta = b_{42}^\Delta = b_{53}^\Delta = b_{54}^\Delta = -\frac{i}{v^2} [2\beta_i^2 \xi_{1i} \sin x_{1i} \cos x_{2i} + (2\beta_i^2 - v^2)/\xi_{2i} \sin x_{2i} \cos x_{1i}] \quad (\text{S44})$$

$$\begin{aligned} b_{33}^\Delta = b_{44}^\Delta &= \frac{1}{v^4 \xi_{1i} \xi_{2i}} [4\zeta_{1i} \zeta_{2i} \beta_i^2 (v^2 - 2\beta_i^2) (\cos x_{1i} \cos x_{2i} - 1) \\ &+ (4\beta_i^4 + v^4 + 4\xi_{1i}^2 \xi_{2i}^2 \beta_i^4 + 4\beta_i^2 v^2) \sin x_{1i} \sin x_{2i}] + 1 \end{aligned} \quad (\text{S45})$$

$$b_{34}^\Delta = b_{43}^\Delta = b_{33}^\Delta - 1 \quad (\text{S46})$$

$$b_{51}^\Delta = b_{62}^\Delta = \frac{i\rho_i}{v^2 \xi_{2i}} [(4\beta_i^4 - 4\beta_i^2 v^2 + v^4) \sin x_{2i} \cos x_{1i} + 4\beta_i^4 \xi_{1i} \xi_{2i} \sin x_{1i} \cos x_{2i}] \quad (\text{S47})$$

$$b_{52}^\Delta = \xi_{1i}/\xi_{2i} \sin x_{1i} \sin x_{2i} \quad (\text{S48})$$

$$\begin{aligned} b_{61}^\Delta &= -\frac{\rho_i^2}{v^4 \xi_{1i} \xi_{2i}} [8\zeta_{1i} \zeta_{2i} \beta_i^4 (4\beta_i^4 - 4\beta_i^2 v^2 + v^4) (\cos x_{1i} \cos x_{2i} - 1) \\ &- (16\beta_i^8 - 32\beta_i^6 v^2 + 24\beta_i^4 v^4 - 8\beta_i^2 v^6 + v^8 + 16\xi_{1i}^2 \xi_{2i}^2 \beta_i^8) \sin x_{1i} \sin x_{2i}] \end{aligned} \quad (\text{S49})$$

Thus, the reflection and transmission coefficients in equations (S13) and (S14) and the reflection and transmission wave fields in equations (S19) and (S20) can be calculated by using equations (S22) and (S23) as well as equations (S24) to (S49).